Experimental observation of elevated heating in dynamically compressed CH foam

View the article online for updates and enhancements.

You may also like

Experimental observation of elevated heating in dynamically compressed CH foam

K Falk[1,2,3] , **C J Fontes**[4]**, C L Fryer**[4]**, C W Greeff**[4]**, M Holec**[5]**, H M Johns**[4]**,
D S Montgomery**[4]**, D W Schmidt**[4] **and M Šmíd**[1]

[1] Helmholtz-Zentrum Dresden-Rossendorf, Bautzner Landstraße 400, 01328 Dresden, Germany
[2] Technische Universität Dresden, 01062, Dresden, Germany
[3] Institute of Physics of the ASCR, 182 21 Prague, Czech Republic
[4] Los Alamos National Laboratory, Los Alamos, NM 87545, United States of America
[5] Lawrence Livermore National Laboratory, Livermore, CA 94550, United States of America

E-mail: k.falk@hzdr.de

CrossMark

Abstract

We present an experimental result of significantly increased heating in a laser-driven blastwave experiment carried out at the OMEGA laser facility. Abnormally high temperatures were observed in warm dense CH compared to older experiments and theoretical predictions. The higher temperatures in compressed CH were linked to an improved smoothness of the laser intensity profile, which resulted in better efficiency of the drive and coupling of more energy into the system compared to previous similar experiments. Fifteen beams with combined intensity of $\sim 7 \times 10^{14}$ W cm^{-2} and a square intensity profile with 2 ns duration were used to drive a strong shock, which subsequently developed to a blastwave travelling through low density CH foam creating warm dense matter. Multiple diagnostics were used to examine the thermodynamic conditions in the warm dense CH foam. Velocity interferometry (VISAR) and streaked pyrometry (SOP) observed increased blastwave velocities, while x-ray Thomson scattering (XRTS) measured elevated temperatures of $17.5 - 35$ eV in compressed CH foam. The experimental results were compared to hydrodynamic simulations and a potential contribution from x-rays to the elevated temperatures in the dense material was considered.

Keywords: warm dense matter, heat transport, laser plasmas, dynamic compression, shock physics

(Some figures may appear in colour only in the online journal)

1. Introduction

The understanding of thermodynamic properties and dynamic behavior of materials at extreme conditions of high energy density (HED) states is crucial for research in laboratory astrophysics, specifically the cores of Jovian planets, white and brown dwarfs [1–3], and Inertial Confinement Fusion (ICF) [4]. This Warm Dense Matter (WDM) regime is characteristic for moderately high temperatures of 0.1–100 eV, solid densities, and often exists at pressures above 1 Mbar. Under such extreme conditions, ions are strongly correlated and the electron population is partially or fully degenerate, which results in increased challenge for any theoretical model as well as standard experimental diagnostic systems. Specifically, transport of radiation and particles through WDM influences the layer structure and convection of astrophysical objects, and electrical conductivity strongly affects magnetic fields generated by planetary core dynamos [5]. The efficient design of

ICF technology depends on detailed and accurate understanding of transport properties of various dense plasma conditions, including WDM. Both shock compression and fast ignition fusion schemes rely on heating of fusion targets by energy deposition of radiation and particles [6–8].

EOS and transport properties of WDM have been studied extensively using various theoretical and computational tools in past years [9, 10]. Some of the most successful theoretical work include *ab initio* quantum molecular dynamics (QMD) simulations obtaining thermal conductivity of warm dense hydrogen [11], resistivity saturation in warm dense Al [12], and charged particle stopping powers and transport have been described both by using pure theory as well as with molecular dynamics (MD) simulations [13–15]. These theoretical efforts have been complemented with experimental projects designed to directly measure transport properties of electrons in dense plasmas [16, 17] and radiation transport in standard materials [18, 19].

The experiment presented in this article was carried out at the OMEGA laser facility [20] using a novel platform previously developed for a full equation-of-state (EOS) measurement with direct measurements of temperature, density, pressure and shock velocity [21, 22]. The experiment utilised imaging x-ray Thomson scattering (XRTS) for the temperature measurement [23, 24] and velocity interferometry (VISAR) [25] and streaked optical pyrometry (SOP) [26, 27] to obtain the shock velocity. This experiment was performed with SG5 phase plates, and the results were compared to a previous experiment, which was performed in almost identical conditions but with SG4 phase plates. The most striking difference is the temperature difference measured by XRTS, where elevated heating in the compressed CH was much higher than expected. Also higher shock/blastwave velocities were observed after the new SG5 phase plates were used. The analysis of the experimental results was supported by a series of radiation hydrodynamics codes including Cassio developed at the Los Alamos National Laboratory (LANL) [28, 29]. With the aid of these simulations we examined the x-ray emission from the hot layers of the targets near the interaction region with the laser as a potential source of this extra heating in the CH, but the modelled flux appears to be insufficient to cause the elevated temperatures both in the dense CH within the blastwave and ahead of it.

This article breaks down into several sections, where section 2 describes the experimental setup, section 3 then focuses on the experimental results from the XRTS, VISAR and SOP diagnostics. This is followed by section 4 that compares these results to hydrodynamic simulations. A potential contribution to preheat by x-rays generated in the experiment is provided in section 5. The discussion and conclusions come in the final section 6.

2. The experimental setup

The experiment was carried out at the OMEGA laser facility at the University of Rochester [20]. A single shock was driven by a laser-plasma ablation process, which lead

generated dense plasma conditions in the WDM regime. Fifteen of the OMEGA laser beams were overlapped to provide a $\sim7\times 10^{14}$ W cm^{-2} square drive with 2 ns duration. The drive beams were frequency-tripled to give $\lambda = 351$ nm wavelength output and their spatial profile was smoothed with distributed phase plates and polarization rotators to maximize the laser-plasma coupling efficiency [30–32]. As the laser pulse was 2 ns long starting at $t = 0$ ns, the shockwave was only supported by the drive for this time. After that the shock evolved into a blastwave moving by its own inertia. Due to geometrical constraints of the OMEGA target chamber the experiment had to be separated into two different parts. The blastwave velocity was measured in one geometrical configuration. The temperature measurement was carried out separately as it required additional x-ray backlighting and the backlighter package obstructed the VISAR/SOP diagnostics. The laser drive and the main target were kept the same in both configurations ensuring that the same laser-plasma conditions were achieved allowing for a direct comparison of the measurements. The experimental platform demonstrated extremely good shot-to-shot stability [17, 21].

This project was carried out over multiple shot days (experiments) over the period of two years. Several stages of technical development took place over this time interval, including modifications of the diagnostics and improvements in the target design. The laser parameters (the intensity, pulse shape, duration, and spot size) were kept the same throughout the entire campaign to ensure the consistency of the experimental measurement. However, new phase plates (SG5) were introduced before our final shot day. These phase plates provide noticeably smoother intensity profile than the previously used SG4 plates [32]. The drive with SG4 plates in the older experiments was varied with high drive using 450 J/beam resulting in approx. intensity of 1×10^{15} W cm^{-2}, and the low drive was then 250 J/beam giving us approx. 5×10^{14} W cm^{-2}. The new SG5 phase plates gave a larger laser focal spot, which was matched using VisRad simulations [33] to emulate the lower drive with SG4 phase plates. The resultant drive was estimated to be maximum $\sim7.5\times 10^{14}$ W cm^{-2} with these new phase plates that gave us a larger spot size for the given geometrical configuration, so the choice was made to only try reproducing the lower drive after the change of the phase plates.

The target geometry was chosen to be a flat 'sandwich', typically used for EOS measurements. The planar layered structures consisted of 25 μm thick plastic (CH) ablator, 2 μm Au thick coating, 70 μm thick Al pusher and 300 μm thick C_8H_8 polystyrene foam. The primary purpose of the Au layer was to shield x-ray radiation created in the hot plasma within the ablator, which is crucial for this particular experiment, where it is necessary to limit the possibility of radiation induced preheat. The HIPE process was used to manufacture the polystyrene foam targets [34]. Additional shielding in a form of gold cones with several μm of plastic coating was added around the targets to stop any direct optical or x-ray emission from contaminating the signal measured by the diagnostic systems. The direct view of the imaging x-ray spectrometer was obscured by a large tungsten shield with 500 μm $\times$ 500 μm aperture to restrict its view only to the passing blastwave, again
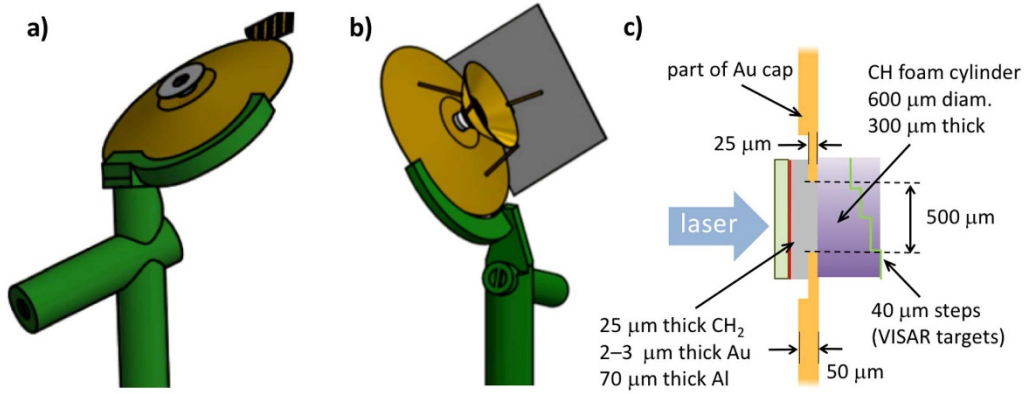
Figure 1. A schematic drawing of the target setup: (a) the overall structure of the VISAR/SOP target with a Au shielding cone and Ta washer that restricts the diagnostic view; (b) XRTS target with additional cones and support structure for the Ni x-ray backlighter, Ta slit setting the scattering angle and W shield for the IXTS diagnostic; (c) the visualisation of the individual layers within the laser-driven package including the 25 μm thick plastic (CH) ablator, 2 μm thick Au coating, 70 μm thick Al pusher and 300 μm thick C_8H_8 polystyrene foam. The schematic also indicates a stepped structure with 40 μm intervals used for the compression wave breakout timing measurements. Adapted figure with permission from [17], Copyright 2018 by the American Physical Society.

to limit any contamination to the scattering signal. The schematics of the target layouts in both geometries are shown in figure 1.

A detailed metrology of the targets and the individual components was carried out in order to reduce any uncertainty in the experimental analysis and target performance. The density of the foam was measured by soft x-ray transmission at 5.4 keV (Cr K-α source) and it was found to be 137.3$\pm$3.5 mg cm^{-3} [35]. The pore sizes were measured with a scanning electron microscope (SEM) obtaining the average pore diameter of 1.26 μm. The size of each step on the back of the CH foam for all VISAR/SOP targets was measured individually with 2 μm accuracy. Special attention was given to the measurement of the thickness for various target components. The Au coating was measured to be 2.02 μm thick with ± 0.01 μm accuracy. An inspection was carried out on the CH ablator material confirming that the thickness was $24 - 25$ μm for all targets used. It was measured to an accuracy of ± 1 μm. These measurements confirmed that the likelihood of the laser burning through the ablator, i.e. hitting the Au directly, or any significantly higher x-ray transmission of the Au layer is very low.

The velocity of the blastwave was obtained by the use of velocity interferometry (VISAR) and streaked optical pyrometry (SOP) diagnostic systems. The two-interferometer line-VISAR system operating at 532 nm at OMEGA was used to provide a continuous temporally and spatially resolved record of the reflected laser emission from the back of the target throughout the duration of the experiment [25]. Since the CH foam is not transparent to light in the optical regime, no direct measurement of the moving shock front was available. Instead, four steps with the height of 40 μm were machined on the back of the foam layer to allow the measurement of blastwave breakout timing that was used to infer velocity of the blastwave though linear interpolation. SOP was used to record a temporally resolved trace of the self-emission from the blastwave front as it broke out across each step at the back of the opaque

target providing complementary velocity measurement [26, 27].

X-ray Thomson scattering (XRTS) was used to obtain high accuracy temperature measurements of the material within the dense shock [23, 36]. The Imaging x-ray Thomson Spectrometer (IXTS), specifically designed for the OMEGA facility for the use of EOS measurements in dense plasmas, was deployed in this experiment [24]. A highly reflective toroidally bent Ge crystal was used to measure the weak scattering signal with excellent spatial resolution. The x-ray backlighter provided Ni He-α emission at 7.78 keV driven by ten 1 ns laser beams with collective intensity of $2 - 3 \times 10^{14}$ W cm^{-2}, focused on a 5 μm thick Ni foil coated on top of a Be support, which also acted as a filter for unwanted low energy emission [37]. No phase plates were used on these beams to ensure maximum intensity with the tight focus. A 200×400 μm Ta slit placed half way in between the Ni foil and the CH foam, which were separated by 1 mm, was used to collimate these x-rays and define the scattering angle to $\sim 100° \pm 5°$. Additional details about the XRTS diagnostic and data analysis for this setup are described in reference [36].

3. Results

The XRTS signal consists of elastic scattering from bound electrons giving the Rayleigh peak at the same energy as the incident x-ray probe, and inelastic scattering from free electrons and bound-free transitions at shifted energies [23]. In the case of non-collective geometry at larger scattering angles, the scattering scale length λ_S is shorter than the plasma screening length λ_D. The scattering is then sensitive to the thermal motion of the individual electrons providing a Compton peak broadened by the thermal distribution of free electrons. The collective geometry, where $\lambda_S > \lambda_D$, results in up and down-shifted plasmon peaks with a profile sensitive to electron density and temperature. This experiment operated in
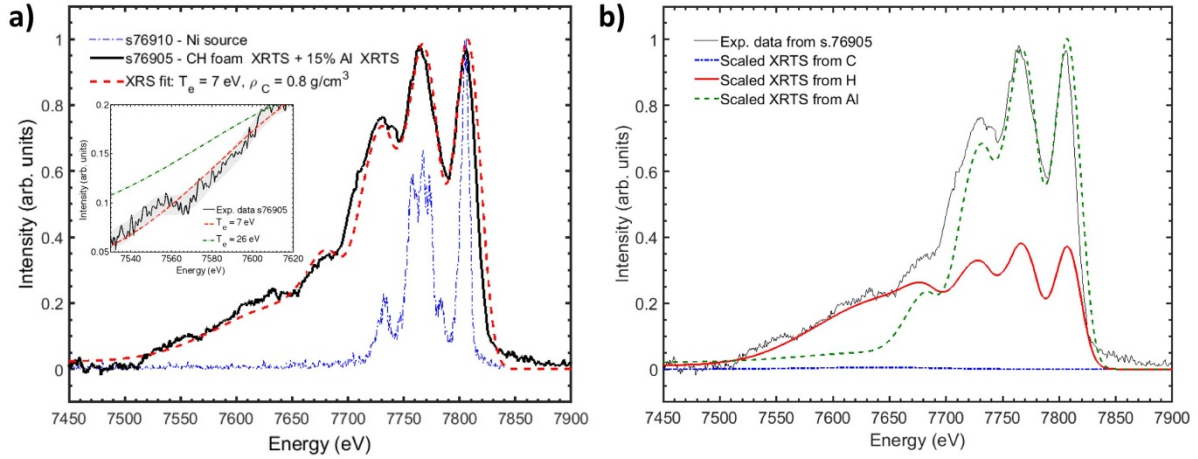
Figure 2. Examples of XRTS data with SG4 phase plates: (a) shows the Ni x-ray backlighter spectrum, raw XRTS data and the composite XRS fit [38]; (b) shows the scaled components of individual contributions from C, H and Al. The estimated conditions used to calculate these profiles were: $T_e = 7$ eV for all, $\rho_C = 0.8$ g cm^{-3}, $Z_C = 2$, $\rho_H = 0.1$ g cm^{-3}, $Z_H = 0.5$, $\rho_{Al} = 1.7$ g cm^{-3}, $Z_{Al} = 3$ respectively. The inset in part (a) shows a detail of the inelastic peak slope to which the fits were compared to obtain the temperature. A slope corresponding to $T_e = 26$ eV measured in equivalent shots with the new SG5 phase plates was added for comparison..

the non-collective regime. The temperature within the dense compressed CH foam in this experiment was obtained using analytically calculated fits to the Compton feature in the XRTS spectra [23]. The XRTS diagnostic only measured the temperature in the compressed CH as the uncompressed foam had too low density to produce detectable scattering signal. The XRS code was used to compute the theoretical fits using a calculation of the structure factors for the specific plasma conditions with the electron temperature T_e, density n_e and ionization state Z as free input parameters [38–40]. These calculations used the measured Ni He-α line emission to generate high accuracy fits that could be directly compared with the experimental scattering spectra. The error bars of the electron temperature measurement were obtained using χ^2 fitting, where T_e and Z were varied for a given n_e value and matched to one standard deviation of the noise in the Compton peak [17].

Prior to the change in phase plates that resulted in different drive coupling to the plasma, our experimental measurements provided a compressed CH temperature of $\sim$7 eV for this system. Figure 2 shows an example of this scattering spectrum. The fit computed by the XRS code [38] was used to extract the temperature as shown in part (a). Unfortunately, this earlier data set was contaminated by scattering from the Al pusher material that was able to expand around the foam sample during the measurement as a result of fault in the target design. Our estimate was that the Al signal made up roughly 15% of the total XRTS signal based on the strength of the Compton peak that comes almost exclusively from C scattering. However, this is just a rough estimate, which is rather difficult to reliably confirm. The individual contributors to the total XRTS signal are shown in figure 2 (b). Each scattering component was calculated separately based on estimated plasma conditions ($T_e = 7$ eV for all, $\rho_C = 0.8$ g cm^{-3}, $Z_C = 2$, $\rho_H = 0.1$ g cm^{-3}, $Z_H = 0.5$, $\rho_{Al} = 1.7$ g cm^{-3}, $Z_{Al} = 3$ respectively) and scaled by the scattering signal intensity,

mass density and spatial extent of the signal with the previously stated assumption of the amount of Al contamination. The figure clearly shows that the Al signal only contributes to the elastic Rayleigh peak while the H scattering is too weak and only acts as continuous broadband background for this geometry and given conditions. The C scattering is then the only component that makes a significant contribution to the Compton peak from which we measure the temperature. Thus, the temperature measurement is unaffected by the Al contamination.

All shots from the last shot day with the new SG5 phase plates were analysed using the XRS code [38]. Examples of such fits to experimental data are shown in figure 3. Scattering measurements have been taken for several shots with the same laser drive probing the shockwave at different probe delay times. The obtained temperatures ranged from 17.5 eV to 35 eV. The full set of measured conditions is provided in table 1. The table is organised in lines for each shot number (first column). The second column shows the delay of the XRTS measurement with respect to the start of the drive at $t = 0$ ns, i.e. the x-ray probe delay. The last two columns then list the temperatures with their error bars extracted from the best XRS fits to each data set [38], and the estimated ionisation degree Z respectively. In data from shots no. 80 373 and 80 377, it was possible to take several different lineouts of the spatially resolved XRTS spectra. Since the integrated signal captured a moving blastwave, we see a spatially smeared time evolution of the temperature. Here the 'lower' lineouts correspond to an earlier time, while the 'upper' lineout data come from x-ray scattering later in the 1 ns long XRTS measurement window.

The values in table 1 are obtained by fitting synthetic spectra with a single set of conditions [38–40]. There is a possibility that the best resolution of the IXTS instrument quoted to be $\sim$20 μm, can be potentially closer to <50 μm under nonideal experimental conditions at OMEGA. We could thus
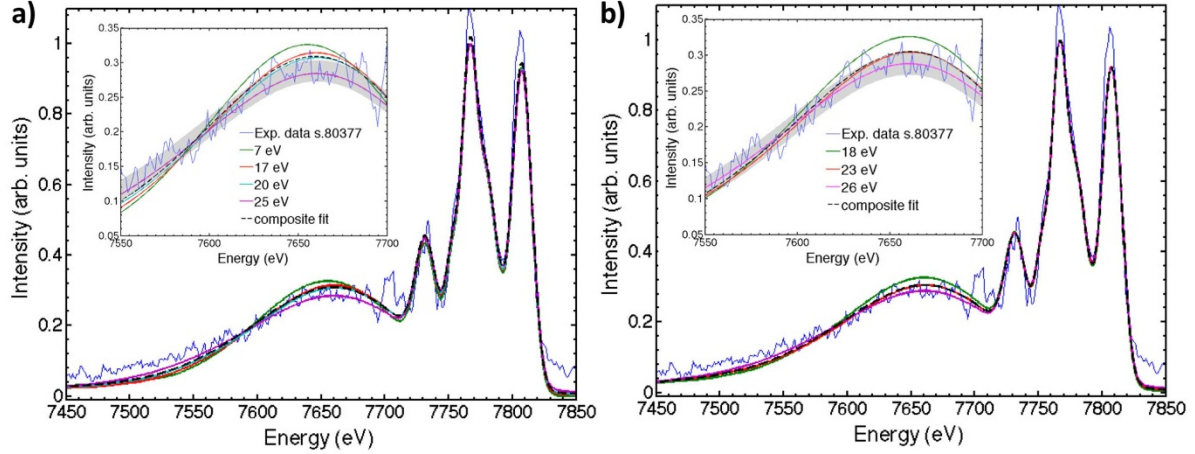
Figure 3. Synthetic XRTS spectral profiles for zones, 1, 2, 3, 4 (a) take across the entire blastwave profile from the simulations and from zones a, b, c (b) using modified thermodynamic conditions overlapped with experimental data. The inset figures show a zoomed in detail of the inelastic scattering peak with the error band corresponding to one standard deviation of the noise level to which the χ^2 fitting was performed. Adapted figure with permission from [17], Copyright 2018 by the American Physical Society.

Table 1. Summary of XRTS results. The time $t = 0$ ns is the start of the laser drive and the delay of the XRTS probe is measured relatively to that.

Shot no. - lineout	XRTS delay	Temperature (T_e)	Z
80 375	5.5 ns	17.5 ± 2.5 eV	2.5
80 373 (lower)	6.0 ns	24.5 ± 4.5 eV	2.2
80 373 (upper)	6.0 ns	27.0 ± 2.5 eV	2.9
80 377 (lower)	6.0 ns	23.0 ± 3.0 eV	2.8
80 377 (middle)	6.0 ns	25.5 ± 2.5 eV	2.8
80 377 (upper)	6.0 ns	26.0 ± 3.0 eV	2.4
80 376	6.5 ns	35.0 ± 5.0 eV	2.2

be integrating the XRTS signal over this distance in the longitudinal direction (i.e. direction of the shock propagation). 2D simulations then confirm that the conditions can be expected to be homogeneous in the transverse direction across which the instrument can provide no spatial resolution. The dense region is expected to be just as homogeneous (probably more) as in previous work using the same platform [22], as the drive and target platform remain unchanged and a thick Al pusher is used this time. To confirm this hypothesis we turn to radiation hydrodynamics simulations and carry out analogous analysis as done in reference [41], where the profile across the spatially integrated region is divided into several sections with some central/averaged conditions. These regional conditions are then used to compute synthetic XRTS spectra ding to:

$$S_{tot}(k,\omega) = \sum_j \rho_j \cdot w_j \cdot S_j(k,\omega), \qquad (1)$$

where ρ_j, w_j and $S_j(k,\omega)$ are the mass density, width and scattering profile of zone j respectively. These profiles were then added up and overlapped with the experimental scattering spectrum. In the first attempt we take into account the possibility that the spectrometer could be integrating over 50 μm instead of the ideal $20 - 25$ μm. We divide the blastwave

region with thickness of $\sim$55 μm into four zones with corresponding temperatures and densities of 1) $T_e = 25$ eV and $\rho = 0.3$ g cm^{-3}, 2) $T_e = 20$ eV and $\rho = 0.25$ g cm^{-3}, 3) $T_e = 17$ eV and $\rho = 0.2$ g cm^{-3}, and 4) $T_e = 7$ eV and $\rho = 0.1$ g cm^{-3} respectively. The result for the individual synthetic spectra overlayed with the experimental result including the composite profile is shown in figure 3 (a).

It is clear that the profile corresponding to the lowest temperature of 7 eV does not fit the new experimental data very well, while the other profiles lay well within the error bars of the original fit presented previously [17]. Thus an additional set of calculations was carried out to obtain more realistic fits that would better match the experimental spectra using a combination of the following three zones of an identical width: (a) $T_e = 18$ eV and $\rho = 0.7$ g cm^{-3}, (b) $T_e = 23$ eV and $\rho = 0.6$ g cm^{-3}, and (c) $T_e = 26$ eV and $\rho = 0.5$ g cm^{-3}. It should be however noted that the XRTS profile is rather insensitive to the density in this configuration and thus density variation does not impact this analysis significantly. The results in figure 3(b) show that all of these conditions can be fitted within the error bars quoted in [17] and thus can be treated as the 'effective temperature' measurements with the central value corresponding to the best fit to the data.

Direct measurements of the blastwave velocity through the breakout timing using the VISAR and SOP diagnostics also revealed surprising findings. Compared to previous data, the blastwaves with improved drive coupling were faster. The blastwave velocities at the break out times for the different shots were found to be 57.8±3.8 km s^{-1}, 64.0±4.9 km s^{-1} and 67.5±5.0 km s^{-1} for the new data respectively. The earlier shots with the SG4 phase plates at low drive, to which we tried to match the new data, gave us shock/blast wave velocities of $40 - 50$ km s^{-1}, while the high drive reached up to $\sim$60 km s^{-1}. The SOP and VISAR diagnostics also found a severe decay in velocity over the time of the measurement. The location of the stepped structure in the target was chosen so that the VISAR/SOP and XRTS measurements would be

equivalent in the temporal evolution of the experiment and the breakout times of the blastwaves were all between 5 and 7 ns from the start of the laser drive at $t = 0$ ns.

In one of the shots after the change of the phase plates, the SOP diagnostic also exhibited direct evidence of increased emission prior to the breakout of the blastwave. This emission could be attributed to preheat increasing the temperature of the material ahead of the shock/blastwave. The conditions of the preheated foam are probably not homogeneous. A reliable opacity model is thus difficult to obtain. An attempt was made to estimate the temperature of the low density foam material ahead of the blastwave using the new calibration of the SOP system at OMEGA [27]. We use the new opacity model for heated CH computed by S. X. Hu *et al* [42] to confirm that even at the elevated temperature, the CH foam remains opaque to optical radiation and thus all observed emission must come from the back surface of the target. The maximum temperatures obtained for a simple black body estimate of the emission from the optically opaque CH foam surface prior the blastwave breakout were within the range of $2.5 - 3.5$ eV. Figure 4 shows the temporal evolution of the temperature obtained from the SOP intensity profile for the shot exhibiting the early emission. The reflectivity of potentially preheated CH was also estimated from simulations by S. X. Hu *et al* [42]. Thus, grey body calculation could also be performed. For CH heated to 2.7 eV at 0.1 g cm^{-3} we get reflectivity $R \sim 0.05$, which does not change the final temperature result in figure 4. For higher potential preheat of 5.4 eV, R climbs up to 0.25, which gives roughly 0.5 eV higher temperatures corresponding to the early emission. The grey band in figure 4 signifies a conservative estimate of the 8% error in the temperature derived from the SOP calibration for blackbody, but it can be up to 17% for grey body calculations [26, 27]. Although this temperature calculation is burdened by many uncertainties and assumptions, it gives us a good estimate of the magnitude of the potential preheat. However, since this was not observed consistently on all shots, this could also be an artefact resulting from for e.g. local density inhomogeneity in that specific target allowing that area to transmit visible radiation and might not prove the existence of preheat.

4. Comparison with simulations

The experimental results were first compared to EOS tables including SESAME 7593 [43] and FPEOS [44] in Hugoniot calculations. Using these, we were able to confirm that reaching higher temperatures would be consistent with higher shock and blastwave velocities of around $70 - 90$ km s^{-1}, which would agree with elevated measured blastwave velocities, but are not in the best agreement with the VISAR/SOP data. The generation of such high velocities with the given drive is unlikely for the given laser drive. The experimental data was then compared with radiation hydrodynamics simulations carried out by the high-energy density code Cassio developed at LANL combining the Radiation adaptive grid Eulerian (RAGE) code [28] coupled with an implicit Monte Carlo treatment [29].
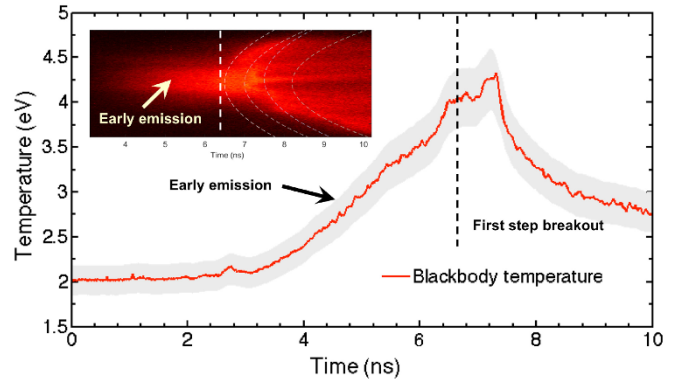

Figure 4. An example of the SOP data showing an evidence of early emission from the foam surface that corresponds to ~ 3 eV temperature.

A 72 energy group structure was used in these simulations and we applied the Rosseland weighting to the OPLIB opacities [45]. These simulations find that the plastic ablator region heats up to temperatures above 100 eV, but no significant amount of x-rays can leak through the Au shield and Al pusher that could cause significant increase of temperature within the shock and blastwave or the preheat the unperturbed foam ahead of it. These simulations predict significantly lower blastwave velocities around $40 - 50$ km s^{-1}, which is consistent with our older data with the SG4 phase plates. Simulations with higher shock velocities that reached higher temperature were carried out, but no contribution of radiation driven preheat due to elevated temperatures in the compressed material was found. A potential preheat due to electrons or x-rays streaming ahead of the shock/blastwave was considered. An artificial preheat of $1 - 10$ eV was introduced to the foam ahead of the blastwave with the assumption that the electron stream would preheat the foam uniformly, see figure 5. With preheat of 10 eV the simulation results better match the higher temperatures within the compressed CH, but such high preheat temperatures appear unreasonable for these conditions as they also correspond to a significant decrease in density of the foam. That is not likely to be the case here as it is not consistent with the XRTS result.

We investigated two methods of calculating the electron thermal conductivity that go beyond the standard Spitzer and Härm treatment [46, 47]. In particular, we considered the approach of Mestel [48], which includes degeneracy effects, and the approach of Hubbard and Lampe [49–52], which also considers degeneracy and is based on a more rigorous treatment of electron-ion and electron-electron scattering. For the present work, we found an increase of $\sim 30\%$ in the electron conductivity of CH at $T = 35$ eV, 0.5 g cm^{-3} and the thermal velocity when comparing the theory of Hubbard and Lampe, or Mestel, to that of Spitzer and Härm.

5. Potential heating contribution from x-rays

Although the Cassio simulation have shown that the preheat caused by x-rays is not likely to happen, this section presents
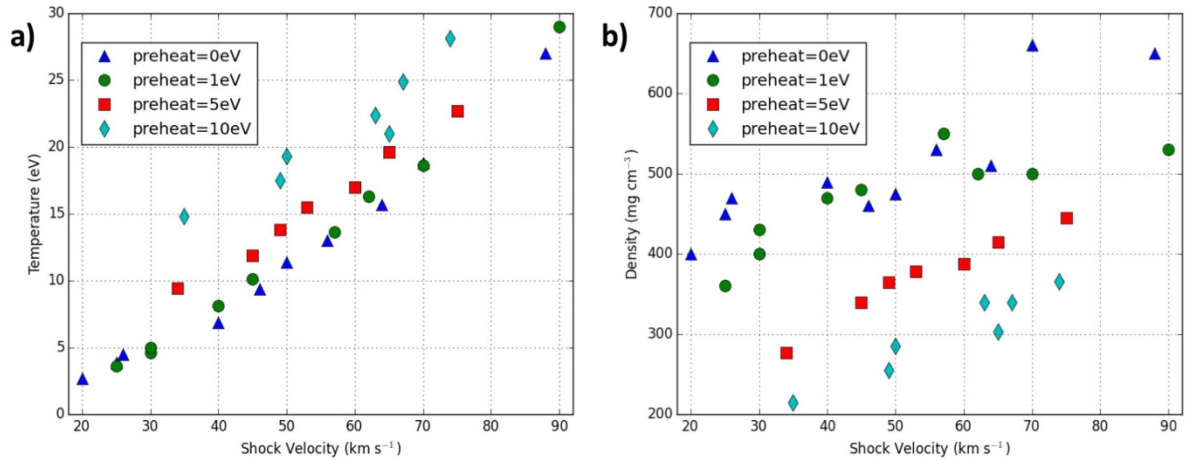
Figure 5. Result of Cassio simulations showing estimated temperature (a) and density (b) in the compressed CH foam as a function of shock velocity for various levels of added preheat increasing the temperature of the unperturbed CH foam 0 eV (no preheat), 1 eV, 5 eV and 10 eV. The simulations used the SESAME 7593 table [43] input with initial foam density of 0.1 g cm^{-3} and varied flux factor.

another approach to understand and exclude the x-ray preheat. The potential contribution to the observed elevated heating in the blastwave and ahead of it was examined using the collisional - radiative atomic code FLYCHK, which calculates the x-ray emission on a detailed level [53, 54]. The plasma parameters from the radiation hydrodynamics simulations for the highly radiative hot plasma (radiation from CH ablator heated to temperature $T = 2$ keV, expanded to density $\rho = 7 \times 10^{-3}$ g cm^{-3} and plasma width $l = 750$ μm, eventually from the heated and expanded Au shield at $T = 35$ eV, $\rho = 1.7$ g cm^{-3}, $l = 20$ μm) were used as an input for the FLYCHK simulations. The transmission through the target (2 μm Au and 70 μm Al) was obtained from the tabulated values [54] and the x-ray flux deposited in the CH foam ahead of the moving shock/blastwave was estimated, see figure 6. X-ray flux deposited in the CH foam was about 0.16 J cm^{-3} for the Au emission, and 25 J cm^{-3} for emission from the CH ablator. The total estimated absorbed x-ray flux is thus 25.16 J cm^{-3}. The effect of the 25.16 J cm^{-3} x-ray flux on the ions in the plasma is at most 0.2 eV of heating. Thus, the upper limit of possible temperature increase by x-ray flux is only 0.02 eV, which is too small to cause significant changes to the temperature of the compressed material or provide preheat measurable by SOP.

6. Discussion and conclusions

The comparison of the two shot days, between which the change from SG4 to SG5 phase plates occurred, was compelling as the target layer structure was identical and the drive intensity was kept the same, thus the difference between those shot days was just the smoothness of the laser spot intensity profile. In the earlier shot day, in which the SG4 phase plates were used, VISAR and SOP diagnostics observed much more steady blastwaves with lower velocities. We did not see a significant increase in blastwave velocities between the low and high drive. This could be an indirect indication that with
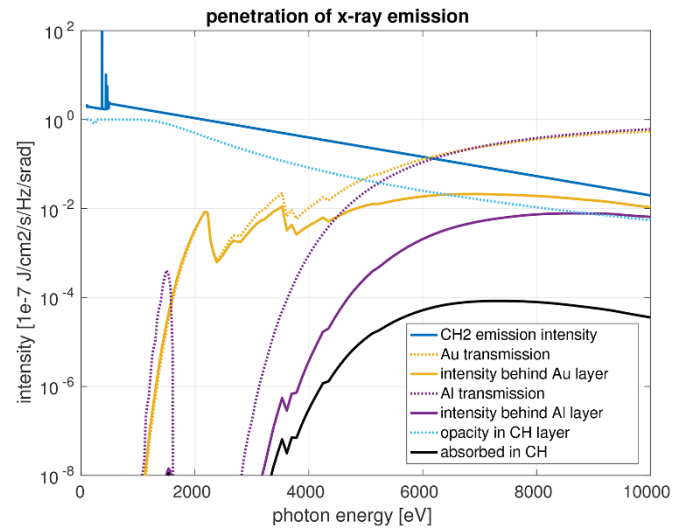

Figure 6. Simulation of x-ray radiation transport. The CH$_2$ ablator emission intensity was propagated through the Al and Au layers while emission from heated and expanded Au was also considered, and the absorption in CH layer was calculated. The spectral integration of this absorption have shown possible heating would be in the order of 0.02 eV.

the older SG4 phase plates the drive was already approaching significant backscattering of the laser light from laser-plasma interactions and increasing the drive had almost no effect as the laser-plasma coupling became highly inefficient. Significantly elevated blastwave velocities of $57.8 - 67.5$ km s^{-1} with a rapid velocity decay were observed after the change to the newer SG5 phase plates, which provided much smoother laser intensity profile. Simultaneously, the x-ray Thomson scattering observed significantly higher temperature in the dense material within the blast wave after the change of the phase plates to SG5. Since such increase was not observed with the higher drive that used the old SG4 phase plates, we can conclude that the smoothness of the laser intensity profile played a dominant role in this change in the blastwave parameters. The

order 1% of the incoming laser energy is needed to heat all of the CH foam to 25 eV. The challenge is to find the channel that can explain not only the heating but also the time dependence.

A comparison with radiation hydrodynamics simulations using the Cassio code was made. These simulations show that for the given Hugoniot conditions, the higher temperatures measured by XRTS would be consistent with higher blastwave velocities in the range of $70 - 90$ km s^{-1}, which is not in agreement with our VISAR/SOP data. In order to match the experimental measurements, artificial preheat of the unperturbed CH ahead of the blastwave was added to the Cassio simulations. It was found that a preheat elevating the unshocked CH temperature to 10 eV could potentially bring up the temperature in the blastwave to the values measured by the XRTS. Our SOP measurements should however support this by an observation of early emission which would indicate that the temperature in the foam was elevated prematurely. While early emission indicating a potentially elevated temperature of $\sim$3 eV was seen on one of the shots, this is however inconclusive and this early emission could attributed to other causes. The potential preheat due to x-ray emission originating in the hot plasma near the critical surface as well as radiation generated within the shock/blastwave itself was studied with the FLYCHK code showing that x-rays are not a potential cause of significant preheat. Initially, we concluded that nonlocal electron transport was responsible for the increased temperatures in the compressed CH [17]. Upon further investigation with multiple simulations and theoretical calculations, it turned out to be an unlikely cause of these higher temperatures. Especially since no conclusive evidence of significant preheat was determined, the mechanism of the elevated heating remains very elusive. Thus, the simulations available to us were unable to match all of the measured data including higher temperatures of compressed CH from XRTS, shock velocities measured by VISAR/SOP and the apparent lack of significant preheat.

The reason for the uncharacteristically higher temperatures in compressed CH thus need to be determined using other models or theories. Also, the effects of improved laser-plasma coupling on the energy transfer within shocked porous materials needs to be better characterised with a set of dedicated experiments. In order to investigate what exactly caused this change, another experiment with specific diagnostics looking at these effects will have to be carried out. The experiment would have to investigate how the new 'extra smoothing' of the laser drive eliminated the loss mechanisms that would reduce energy coupling. There would have to be a full range of diagnostics including XRTS (shock temperature), VISAR (shock velocity), SOP (shock velocity and preheat), x-ray radiography (shock density), light back-scattering diagnostics and electron spectrometers to observe the effects of the laser drive on parametric instabilities, a visible spectrometer, x-ray pinhole cameras and streaked x-ray spectrometers to measure all possible carriers of preheat, energy coupling, and plasma conditions to investigate the energy distribution between the laser and plasma and within the target. Such an experiment would then have to be supported by a detailed model of laser-plasma instabilities. It is also highly likely that the heat diffusion in the

rad. hydro. simulations may not be very accurate, especially not in the dense plasma regime, which is another problem that will have to be tackled in the future.

Since the blastwave is propagating in porous material, it is possible that the thermal part of the energy flux was enhanced in this experiment [55]. The improved laser-plasma coupling could have intensified the effect of anomalous shock compression of the porous substance leading to higher thermal effects in pressure and energy flux. Yet, we have no means to confirm this hypothesis using simulations available to us. We also consider that the irregular porous structure and density gradients in the foam could result in the generation of secondary shockwaves due to the development of vortex or Richtmyer-Meshkov instabilities that could contribute to further collisional heating in the compressed foam. This remains a speculation that should be further explored. Other potential sources of abnormal heating of the CH were considered and they include the situation when the laser would burn through the CH ablator and impacted the Au foil directly, which could lead to a direct x-ray emission. However, our simulations showed that with the given laser intensity and ablator material thickness, such a situation is highly unlikely. There is also a possible effect of refluxing of energetic electrons originating from the laser-plasma interaction that could cause additional heating in the target without the decrease in CH density, which would be consistent with the measured data. At our drive intensity of $\sim$7$\times$ 10^{14} W cm^{-2}, one can assume that $1 - 3\%$ of the laser energy goes into hot electrons with a $T_{hot} \sim 80 - 100$ keV [56, 57]. Such hot electrons are usualy generated in laser plasma instabilities driven by laser parametric instabilities resulting from high intensity spikes in the laser drive. The SG5 phase plates provided a smoother laser intensity profile which should reduce these instabilities and therefore fewer hot electrons should be produced. However, a change in the speckle pattern could still result in unexpected outcomes. A detailed modelling and direct measurement of fast electron preheat is thus needed before fast electrons can be discounted as a potential cause of the observed extra heating.

The data presented in this article comparing measurements of plasma conditions in a laser-driven shock/blastwaves with two different laser intensity profiles lead us to the conclusion that the change to the improved SG5 phase plates, which provided a smoother drive profile, resulted in an improved efficiency of the laser-target interaction, probably by reducing the effect of laser-plasma instabilities. With this more efficient drive, we were able to couple more energy into the system and reach different plasma conditions. While the higher blastwave velocities could be directly explained by better laser-plasma coupling with our theoretical models, we find inconsistencies in the measured temperatures in the blastwave and the Cassio simulations. After excluding the preheat by x-rays as a potential cause of these elevated temperatures, we are left with few potential explanations and speculations. While it is evident the gradual increase of temperature with time is due to the improved coupling provided by the SG5 phase plates, the direct mechanism is not yet understood. The process responsible for the elevated temperatures observed by XRTS and higher shock velocities is not captured in the theoretical

models available to us. This could be of some concern to the community and other models should be tested, whether they can reproduce the experimental data presented here in a better manner. It calls for further theoretical and experimental exploration of these effects. It is important for our ability to understand and predict experiments in ICF, HED, EOS and WDM laser driven experiments so that as experimental capabilities evolve we continue to maintain our ability to understand the underlying physical processes.

Acknowledgment

ORCID iD

K Falk ⬤ https://orcid.org/0000-0001-5975-776X

References

[1] Lebedev S 2007 *High Energy Density Laboratory Astrophysics* (Berlin: Springer) (https://doi.org/10.1007/978-1-4020-6055-7)

[2] Guillot T 1999 Interiors of Giant Planets Inside and Outside the Solar System *Science* **286** 72–7

[3] Hurricane O *et al* 2014 Fuel gain exceeding unity in an inertially confined fusion implosion *Nature* **506** 343

[4] McCrory R L *et al* 2005 Direct-drive inertial confinement fusion research at the Laboratory for Laser Energetics: charting the path to thermonuclear ignition *Nucl. Fusion* **45** S283

[5] Olson P 2013 The New Core Paradox *Science* **342** 431

[6] Humphries Jr S 1980 Intense pulsed ion beams for fusion applications *Nucl. Fusion* **20** 1549

[7] Tabak M *et al* 1994 Ignition and high gain with ultrapowerful lasers *Phys. Plasmas* **1** 1626

[8] Goncharov V N *et al* 2006 Early stage of implosion in inertial confinement fusion: Shock timing and perturbation evolution *Phys. Plasmas* **13** 012702

[9] Driver K P and Militzer B 2012 All-Electron Path Integral Monte Carlo Simulations of Warm Dense Matter: Application to Water and Carbon Plasmas *Phys. Rev. Lett.* **108** 115502

[10] Saumon D, Starrett C E, Kress J and Clerouin J 2012 The quantum hypernetted chain model of warm dense matter *HEDP* **8** 150

[11] Recoules V *et al* 2009 Ab Initio Determination of Thermal Conductivity of Dense Hydrogen Plasmas *Phys. Rev. Lett.* **102** 075002

[12] Faussurier G and Blancard C 2015 Resistivity saturation in warm dense matter *Phys. Rev.* E **91** 013105

[13] Li C K and Petrasso R D 1993 Charged-particle stopping powers in inertial confinement fusion plasmas *Phys. Rev. Lett* **70** 3059

[14] Li C K and Petrasso R D 2015 Erratum: Charged-Particle Stopping Powers in Inertial Confinement Fusion Plasmas [Phys. Rev. Lett. 70, 3059 (1993)] *Phys. Rev. Lett* **114** 199901(E)

[15] Grabowski P E *et al* 2013 Molecular Dynamics Simulations of Classical Stopping Power *Phys. Rev. Lett.* **111** 215002

[16] Pasley J *et al* 2007 Experimental observations of transport of picosecond laser generated electrons in a nail-like target *Phys. Plasmas* **14** 120701

[17] Falk K *et al* 2018 Measurement of Preheat Due to Nonlocal Electron Transport in Warm Dense Matter *Phys. Rev. Lett.* **120** 025002

[18] Falize E, Michaut C and Bouquet S 2011 Similarity properties and scaling laws of radiation hydrodynamic flows in laboratory astrophysics *Astrophys. J.* **730** 96

[19] Rosen P A *et al* 2009 Laboratory experiments to study supersonic astrophysical flows interacting with clumpy environments *Astrophys. Space Sci* **322** 101

[20] Boehly T R *et al* 1997 Initial performance results of the OMEGA laser system *Opt. Commun* **133** 495

[21] Falk K *et al* 2014 Equation of State Measurements of Warm Dense Carbon Using Laser-Driven Shock and Release Technique *Phys. Rev. Lett.* **112** 155003

[22] Falk K *et al* 2014 Combined x-ray scattering, radiography, and velocity interferometry/streaked optical pyrometry measurements of warm dense carbon using a novel technique of shock-and-release *Phys. Plasmas* **21** 056309

[23] Glenzer S H and Redmer R 2009 X-ray Thomson scattering in high energy density plasmas *Rev. Mod. Phys.* **81** 1625

[24] Gamboa E J *et al* 2012 Imaging x-ray Thomson scattering spectrometer design and demonstration *Rev. Sci. Instrum.* **83** 10E108

[25] Celliers P M *et al* 2004 Line-imaging velocimeter for shock diagnostics at the OMEGA laser facility *Rev. Sci. Instrum.* **75** 4916

[26] Miller J E *et al* 2007 Streaked optical pyrometer system for laser-driven shock-wave experiments on OMEGA *Rev. Sci. Instrum.* **78** 034903

[27] Gregor M C *et al* 2016 Absolute calibration of the OMEGA streaked optical pyrometer for temperature measurements of compressed materials *Rev. Sci. Instrum.* **87** 114903

[28] Gittings M *et al* 2008 The RAGE radiation-hydrodynamic code *CS & D* 1 **63** 015005

[29] Urbatsch T J and Evans T M 2005 Milagro Version 2, An Implicit Monte Carlo Code for Thermal Radiative Transfer: Capabilities, Development, and Usage Los Alamos National Laboratory Report LA-14195-MS

[30] Kruer W L 2003 *The Physics of Laser Plasma Interactions* (Westview, Colorado)

[31] Lin Y, Kessler T J and Lawrence G N 1995 Distributed phase plates for super-Gaussian focal-plane irradiance profiles *Opt. Lett.* **20** 764

[32] Regan S P *et al* 2005 Performance of 1-THz-bandwidth, two-dimensional smoothing by spectral dispersion and polarization smoothing of high-power, solid-state laser beams *J. Opt. Soc. Am.* B **22** 998

[33] MacFarlane J and Quant J 2003 VISRAD—A 3-D view factor code and design tool for high-energy density physics experiments *Spectr. Rad. Transfer* **81** 287

[34] Williams J M and Wrobleski D A 1988 Spatial distribution of the phases in water-in-oil emulsions. Open and closed microcellular foams from cross-linked polystyrene *Langmuir* **4** 3

[35] Lanier N E, Hamilton C and Taccetti J M 2012 A monochromatic x-ray imaging system for characterizing low-density foams *Rev. Sci. Instrum.* **83** 10E520

[36] Falk K *et al* 2017 X-ray Thomson scattering measurement of temperature in warm dense carbon *Plasma Phys. Control. Fusion* **59** 014050

[37] Workman J and Kyrala G A 2001 Scaling of x-ray K-shell sources from laser-solid interactions *Proc. SPIE* vol 4504 pp 168–79

[38] Gregori G *et al* 2007 Derivation of the static structure factor in strongly coupled non-equilibrium plasmas for X-ray scattering studies *HEDP* **3** 99

[39] Gregori G and Gericke D O 2009 Low frequency structural dynamics of warm dense matter *Phys. Plasmas* **16** 056306

[40] Gericke D O, Vorberger J, Wünsch K and Gregori G 2010 Screening of ionic cores in partially ionized plasmas within linear response *Phys. Rev.* E **81** 065401(R)

[41] Falk K *et al* 2013 Comparison between x-ray scattering and velocity-interferometry measurements from shocked liquid deuterium *Phys. Rev.* E **87** 043112

[42] Hu S X *et al* 2017 Optical properties of highly compressed polystyrene: An ab initio study *Phys. Rev.* B **96** 144203

[43] Lyon S P and Johnson J D 1992 Sesame: The Los Alamos National Laboratory equation of state database Los Alamos National Laboratory Report LA-UR-92-3407

[44] Hu S X *et al* 2015 First-principles equation of state of polystyrene and its effect on inertial confinement fusion implosions *Phys. Rev.* E **92** 43104

[45] Colgan J *et al* 2016 A new generation of los alamos opacity tables *Astrophys. J.* **817** 116

[46] Spitzer Jr L and Härm R 1953 Transport Phenomena in a Completely Ionized Gas *Phys. Rev.* **89** 977–81

[47] Spitzer Jr L 1962 *Physics of Fully Ionized Gases.* ed 2nd (New York, London: Interscience Publ. Inc)

[48] Mestel L 1950 On the thermal conductivity in dense stars *Proc. Cambridge Phil. Soc.* 46 331–8

[49] Hubbard W B 1966 Studies in Stellar Evolution. V. Transport Coefficients of Degenerate Stellar Matter *Astrophys. J.* **146** 858–70

[50] Lampe M 1968 Transport Coefficients of Degenerate Plasma *Phys. Rev* **170** 306–19

[51] Lampe M 1968 Transport Theory of a Partially Degenerate Plasma *Phys. Rev* **174** 276–89

[52] Hubbard W B and Lampe M 1969 Thermal Conduction by Electrons in Stellar Matter *Astrophys. J. Suppl. Ser* **18** 297–346

[53] Chung H-K *et al* 2005 FLYCHK: Generalized population kinetics and spectral model for rapid spectroscopic analysis for all elements *High Energy Density Physics* **1** 3

[54] Henke B L, Gullikson E M, Davis J C, Data A and 1993 X-Ray Interactions: Photoabsorption, Scattering, Transmission, and Reflection at E = 50-30,000 eV, Z = 1-92 *Nucl. Data Tables* **54** 181–342

[55] Fortov V E and Lomonosov I V 2014 Ya B Zeldovich and equation of state problems for matter under extreme conditions *Physics - Uspekhi* **57** 219–33

[56] Froula D H *et al* 2012 Saturation of the Two-Plasmon Decay Instability in Long-Scale-Length Plasmas Relevant to Direct-Drive Inertial Confinement Fusion *Phys. Rev. Lett.* **108** 165003

[57] Michel D T *et al* 2013 Measured hot-electron intensity thresholds quantified by a two-plasmon-decay *Phys. Plasmas* **20** 055703